Activation Kinetics of the Boron–oxygen Defect in Compensated n- and p-type Silicon Studied by High-Injection Micro-Photoluminescence

Chang Sun, Hieu Trong Nguyen, Hang Cheong Sio, Fiacre Emile Rougieux, and Daniel Macdonald

Abstract—*In situ* measurement of the activation kinetics of the slowly forming recombination center (SRC) of the boron–oxygen defect in compensated n- and p-type silicon (n-Si and p-Si) under high-injection conditions is realized through micro-photoluminescence measurements. The high-injection conditions significantly accelerate the defect activation. Another advantage of this method is that the injection level can be kept almost constant during the defect activation and in differently doped samples, as the high-injection lifetime is dominated by Auger recombination. Courtesy of this, the activation time constant remains steady during the activation of the defects, and the activation time constant and defect concentration in differently doped samples can be compared more directly. The results confirm that the defect activation rate constant is the same at high-injection levels in both n- and p-type samples, and that it only depends on the hole concentration p, but not on $[O_i]$ or $[B]$. The effective saturated defect concentration normalized with $[O_i]^2$ is independent of the doping in n-Si, and increases with the net doping in p-Si. The latent form reconfiguration model for the defect, instead of the B_s–O_{2i} model, is considered to be more compatible with these findings.

Index Terms—Boron oxygen (BO) defects, compensated, Czochralski silicon (Cz-Si), light-induced degradation, photoluminescence (PL).

I. INTRODUCTION

THE boron–oxygen (BO) defect, which causes degradation of carrier lifetimes in boron-doped oxygen-rich Czochralski silicon (Cz-Si) under illumination, has been studied intensely in recent years [1]–[11]. A common method to study the activation kinetics of the defect is to illuminate a wafer with a lamp and then measure the lifetime, under moderate injection levels, from which an effective value of the defect concentration can be extracted [1]. This method is, however, affected by the following issues:

① The lamp illumination can typically only reach several suns or lower in most cases, so only low to medium injection levels can be achieved during defect activation, which results in slow activation rates in compensated n-Si [2]–[5].

② During the activation of the BO defect, the lifetime degrades significantly, resulting in a strongly varying injection level over time when the illumination intensity is fixed. This creates a further complication in modeling the kinetics because the reaction rate constant is known to depend on the carrier densities [4]–[6].

③ Samples with different net dopings will have different lifetimes, leading to different injection levels when using the same illumination source [3], [7], [8]. As a result it is difficult to discriminate the effects of the net doping and the injection level on the activation rate, which could lead to different interpretations [4], [6].

④ The effective defect density is usually obtained in low or medium injection using the inverse lifetime at $\Delta n = \eta N_{A/D}$ (η is constant). However, this approach does not necessarily properly account for the effects of the net doping on the effective defect concentration in the Shockley–Read–Hall (SRH) model (or multivalent defect lifetime model) [12]–[14]. This is an unavoidable problem when comparing n-Si and p-Si [5]. It also introduces uncertainties when comparing one type of silicon with different doping levels, as the relevant deep levels reported in some works do not necessarily result in negligible n_1 or p_1 [9], [10].

One way to address these issues is to activate the BO defects under high-injection. First, it results in faster activation rates which address the aforementioned issue ①. Also, at sufficiently high-injection levels, the effective lifetime will be Auger recombination limited, and thus it is not as sensitive to the SRH recombination as it is at low to medium injection levels. This potentially addresses issue ②. In addition, differently doped samples will have similar high-injection Auger lifetimes, resulting in similar injection levels when fixing the illumination intensity, addressing issue ③. Finally, defect concentrations in differently doped samples can be conveniently compared, if they are derived from the high-injection SRH lifetime, which is independent of the net doping, addressing issue ④.

In this work, a micro-photoluminescence (micro-PL) system with confocal optics is applied to study the activation kinetics of the BO defect. High-injection conditions are realized by an intense laser spot only several microns in diameter. The *in situ* measurement of the kinetics is realized by capturing the PL signal at close time intervals, with the laser illumination on all

TABLE I
[B] AND [P] IN THE STARTING MELT OF THE INGOTS, AND THE SOLIDIFIED FRACTIONS g, NET DOPING LEVELS n_0 OR p_0, AND [O_i] OF THE SAMPLES

	[B] in the starting melt ($\times 10^{16}$ cm^{-3})	[P] in the starting melt ($\times 10^{16}$ cm^{-3})	Range of g	Number of samples	Range of n_0 in n-type samples ($\times 10^{15}$ cm^{-3})	Range of p_0 in p-type samples ($\times 10^{15}$ cm^{-3})	[O_i] ($\times 10^{17}$ cm^{-3})
Ingot 1	3.0	2.9	$0.05 - 0.97$	18	1.6 - 41	2.3 - 10	6.5
Ingot 2	6.2	10 (± 1)	$0.05 - 0.78$	18	1.3 - 33	$0.044 - 4.9$	$6.1 - 9.1$

the time. With this method, we measure and model the kinetics of the BO defect activation in both compensated n- and p-Si. Based on the results we discuss some unresolved issues related to the defect.

II. EXPERIMENTS

A. Sample Preparation

The samples were from two B- and P-doped compensated Czochralski (Cz) ingots. Samples from different solidified fractions g were selected for this study. The concentrations of B and P ([B] and [P]) in the starting melt of the ingots, and the ranges of g are shown in Table I. The [B] and [P] in the samples were calculated by applying the Scheil law. The segregation coefficients of B and P were taken as 0.75 and 0.41, respectively [3]. The predicted ranges of n_0 or p_0 in the samples are shown in Table I. In [3], the [B] and [P] in some of the samples were measured by secondary ion mass spectrometry, and the net doping was measured by electrochemical capacitance voltage measurements. Refer to [3] for more detailed analysis on the doping levels and the uncertainties in the predictions by applying the Scheil law. The interstitial oxygen concentrations ([O_i]) were determined by Fourier transform infrared spectrophotometry [2], and the results are also shown in Table I. The samples were chemically etched to remove saw damage, and then went through a phosphorus gettering process at 880 °C for 0.5 h in 4.4 L/min nitrogen, 0.1 L/min oxygen, and 15 ml/min POCL3, and at 600 °C for about 14 h in nitrogen ambient [15], to remove fast diffusing metallic impurities. The diffusion layers were then removed, followed by surface passivation with plasma-enhanced chemical vapor deposited silicon nitride films. All samples had identical thermal history during the processing. Before the measurements, the samples were annealed at 260 °C for 40 min in dark to completely deactivate the BO defects.

A p-type B-doped float-zone (FZ) wafer with $N_A = 8 \times 10^{15}$ cm^{-3}, and an n-type P-doped FZ wafer with $N_D = 5 \times 10^{15}$ cm^{-3} were also included in this study. The doping levels in these samples were determined by dark conductance measurements. The samples were also chemically etched and passivated with the same silicon nitride films.

B. Micro-PL Measurements

The micro-PL system used in this study was a Horiba LabRAM system equipped with a confocal microscope. The excitation wavelength of the incident laser beam was 532 nm. The on-sample size of the laser beam was about 2.5 μm in diameter, and the on-sample illumination power was about 42 mW. The emitted PL signal was focused through a square pinhole located in front of a monochromator and an InGaAs array de-
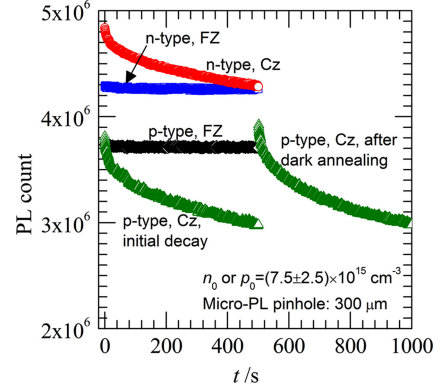

Fig. 1. PL count as a function of time measured on the FZ samples, a p-type Cz sample from Ingot 1 ($g = 0.27$) and an n-type Cz sample from Ingot 2 ($g = 0.52$). Another set of PL intensities measured at the same location on the p-type Cz sample after dark annealing is also shown. The pinhole size of the micro-PL system was 300 μm in this case. Note that the vertical axis does not start from 0.

tector. The detected area on the sample surface was determined by the adjustable pinhole size and the objective lenses. Two pinhole sizes 200 and 300 μm were used in this work. These values represent the length of the side of the square pinholes. The corresponding detection area on the sample surface is measured in Section III-B. Note that adjusting the pinhole sizes will only affect the region seen by the detector, but not the illumination and the emission of the signal.

All measurements were performed at room temperature. The integrated band-to-band PL signal from one spot was measured on each sample, with a 0.5 s time step. The acquisition time for collecting each signal was 0.3 s. The laser remained on all the time. This allowed *in situ* monitoring of the PL signal during the activation of BO defects.

To confirm that the observed PL signal degradation is indeed caused by the activation of the BO defect, we annealed a p-type sample from $g = 0.27$ of Ingot 1 at 260 °C for 40 min in dark using the *in situ* temperature-controlled stage of the system after performing a degradation measurement for 500 s. This allowed complete deactivation of the BO defect after intentional degradation with the laser. We were then able to perform another measurement at exactly the same spot, after cooling the sample down to room temperature.

III. RESULTS, MODELING, AND DISCUSSION

A. Confirming the BO Defect

Fig. 1 shows the PL count as a function of time measured on the two FZ wafers and two compensated Cz samples. The PL count is a unitless value which is proportional to the number of
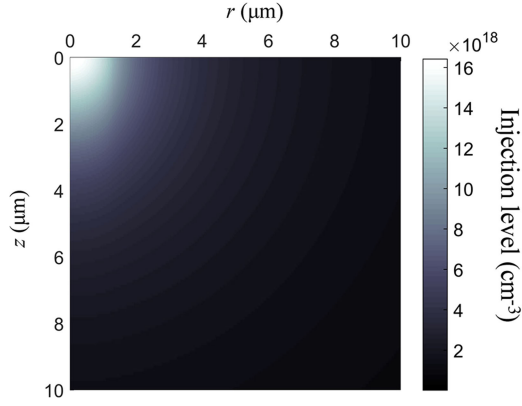
This article has been accepted for inclusion in a future issue of this journal. Content is final as presented, with the exception of pagination.

SUN *et al.*: ACTIVATION KINETICS OF THE BORON–OXYGEN DEFECT IN COMPENSATED N- AND P-TYPE SILICON
3

Fig. 2. Modeled injection level. r is parallel with the sample surface, and z is the direction of the depth. (0, 0) is the center of the illumination spot on the sample surface.

photons detected by the detector within the acquisition time. An obvious degradation of the PL signal of both Cz samples can be seen. The PL signal of the FZ samples remains steady during the measurement. The illumination intensity is steady over time as monitored by a power meter. We can then conclude that 1) the surface passivation is stable upon illumination; and 2) the defects causing the PL degradation in the Cz samples do not exist in the FZ samples. The PL signal measured at the same location on the p-type Cz sample after the dark annealing is also shown in the figure; the result confirms that the defect can be deactivated by the dark annealing. Thus, we concluded that the PL signal degradation is caused by the activation of the BO defect [1].

B. Modeling the Injection Level During the Measurement and Determining the Detection Profile of the Micro-PL System

The injection level in a p-type sample with $p_0 = 5 \times 10^{15}$ cm^{-3} and $\tau_{\mathrm{SRH}} = 200\,\mu$s during the *in situ* measurement is simulated, using a three-dimensional finite element method [16], [17]. Greater detail of the model will be included in future publications. Fig. 2 shows the simulated Δn as a function of the depth z, and the lateral distance from the center of the illuminated spot on the sample surface r. Line scans of $\Delta n(r)$ at $z = 0$ and $\Delta n(z)$ at several r values are shown in Fig. 3. The injection profile shown in the figures is a result of carrier diffusion from the illumination spot, the center of which is at (0, 0). As shown by the modeling results, in most of the area where r, $z < 100\,\mu$m, the injection is in the range of $10^{17} - 10^{18}$ cm^{-3}, satisfying the high-injection condition ($\Delta n \gg n_0$ or p_0) for the samples in this work. In addition, the simulated Δn in this area is found to vary only slightly for τ_{SRH} values higher than $10\,\mu$s, and for net doping levels lower than 5×10^{16} cm^{-3}. This also indicates that the high-injection condition prevails in this area, and that the effective lifetime of this area is dominated by the Auger lifetime.

The detection profile (on the sample surface) of the micro-PL system is measured by mapping a point light source which is $1\,\mu$m in diameter, using a silicon detector [16]. The step size in both lateral directions (x and y) in the mapping is $1\,\mu$m. Fig. 4 shows the normalized detection sensitivity for two pinhole sizes,
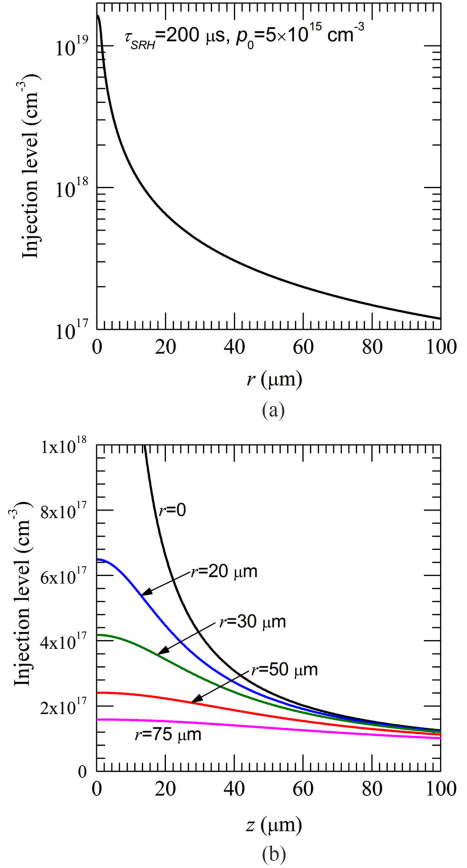

Fig. 3. (a) The injection level as a function of r at the sample surface ($z = 0$), and (b) as a function of z at different r values.

200 and 300 μm. As shown by the figure, the detection area on the sample surface is approximately square. In the vertical direction (the depth z), in principle, all the photons that reach the sample surface and are emitted within the detection area on the sample surface should be detected. In [16], the detection profile in the depth direction is also measured by scanning the light source, showing that the detection sensitivity vanishes within tens of microns from the sample surface for both 100 and 1000 μm pinhole sizes. In this work, we can safely assume that the detected PL signal mainly comes from the area where $z < 100\,\mu$m.

The modeled injection level and the measured detection profile of the micro-PL system show that in the detection area, the injection level is extremely nonuniform. Using the 300 μm pinhole, for instance, the injection level varies by approximately two orders of magnitude. This will complicate the study of the activation kinetics of the BO defect. To reduce this effect, in this study we use both pinhole sizes, 200 and 300 μm, to conduct two *in situ* measurements for each sample. Then we subtract the PL signals from both measurements for the quantitative analysis. The subtracted PL signal comes from an area where 30 μm $< r < 75\,\mu$m, and $z < 100\,\mu$m. The schematic of the area on the sample surface is illustrated in Fig. 4(c). This narrows down the range of the injection level to about $1 \times 10^{17} - 4 \times 10^{17}$ cm^{-3}, while the high-injection condition still holds approximately. Although choosing two closer pin
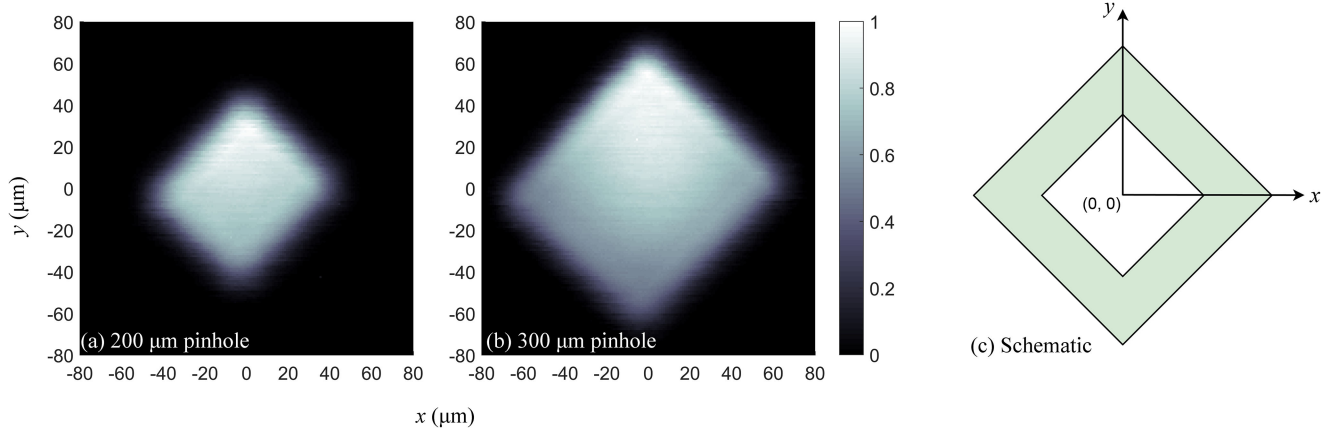
Fig. 4.   Detection profiles on the sample surface when the pinhole size of the micro-PL system is set as (a) 200 μm, (b) 300 μm, and (c) schematic of the resultant area when subtracting the PL signal from both measurements using 200 and 300 μm pinholes.
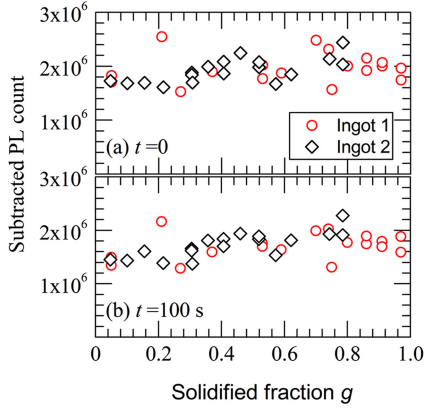

Fig. 5.   Subtracted PL count at $t = 0$ and 100 s measured on all the Cz samples.

TABLE II
PREDICTED ACTIVATION TIME CONSTANTS OF THE FRC AND SRC

Δn (cm^{-3})	$\tau_{\mathrm{gen}}^{\mathrm{FRC}}$ (s)	$\tau_{\mathrm{gen}}^{\mathrm{SRC}}$ (s)
1×10^{17}	0.2	132
2×10^{17}	0.05	33
3×10^{17}	0.02	14.67
4×10^{17}	0.0125	8.25
5×10^{17}	0.008	5.3

At high-injection levels, $n = p = \Delta n$.

hole sizes will further narrow down the injection range, the subtracted PL signal also becomes much noisier, which negatively affects the analysis.

C. Experimentally Confirming the Fixed High-Injection Condition Over Time and in Different Samples

To further confirm the high-injection condition in the studied area ($30\,\mu$m $< r < 75\,\mu$m, $z < 100\,\mu$m), we compare the subtracted PL count at $t = 0$ and 100 s measured on all the Cz samples, as shown in Fig. 5. Comparing all the samples at $t = 0$ [see Fig. 5(a)], the PL count does not vary much, although they have significantly varying net doping levels. It indicates that high-injection condition prevails such that [18]

$$I_{\mathrm{PL}} = A_i \cdot B \cdot \Delta n^2. \qquad (1)$$

Furthermore, courtesy of the high-injection condition, the effective lifetime is dominated by Auger recombination, and thus is much less sensitive to the activation of the BO defects. It explains why the PL signal of the Cz samples does not degrade significantly before it almost saturates as shown in Fig. 1. Fig. 5(b) further demonstrates this point by showing the PL count of each sample at $t = 100$ s. Therefore, an approximately steady high-injection condition over time and across different samples is

established. As estimated based on (1), in 100 s, the change in the injection level is at most 12%, and 6% on average across all the samples.

D. Extracting the Effective Defect Concentration of the SRC

The activation time constants of the fast- and slowly forming recombination centers (FRC and SRC) are predicted based on [4]–[6], as shown in Table II. The explicit equations for the calculations can be found in [5]. We assume that the equations in [5] hold for high-injection levels. We can see that at high-injection levels the activation of the FRC becomes so fast that it is likely to have saturated at the first measured point. The high-injection recombination lifetime of the FRC is usually more than one order of magnitude higher than SRC [6], so the activation of the FRC will not, in any case, have a significant impact on the observed change in the PL signal. Therefore, in the following discussion we will only consider the activation of the SRC, which causes the PL signal degradation over the measured time scale.

In this work we extract the effective defect concentration assuming that the injection level is approximately uniform in the detected area. The effects of the nonuniformity of the injection are discussed in greater detail in the following sections. With a steady generation rate, $\Delta n = \tau_{\mathrm{eff}} \cdot G$. Combining with (1), we have $I_{\mathrm{PL}} \propto \tau_{\mathrm{eff}}^2$, from which a relative value of τ_{eff} can be derived. The recombination lifetime of the SRC, τ_{SRC} can then be extracted by applying $1/\tau_{\mathrm{SRC}}(t) = 1/\tau_{\mathrm{eff}}(t) - 1/\tau_{\mathrm{eff}}(t = 0)$ [1].

This article has been accepted for inclusion in a future issue of this journal. Content is final as presented, with the exception of pagination.

SUN *et al.*: ACTIVATION KINETICS OF THE BORON–OXYGEN DEFECT IN COMPENSATED N- AND P-TYPE SILICON
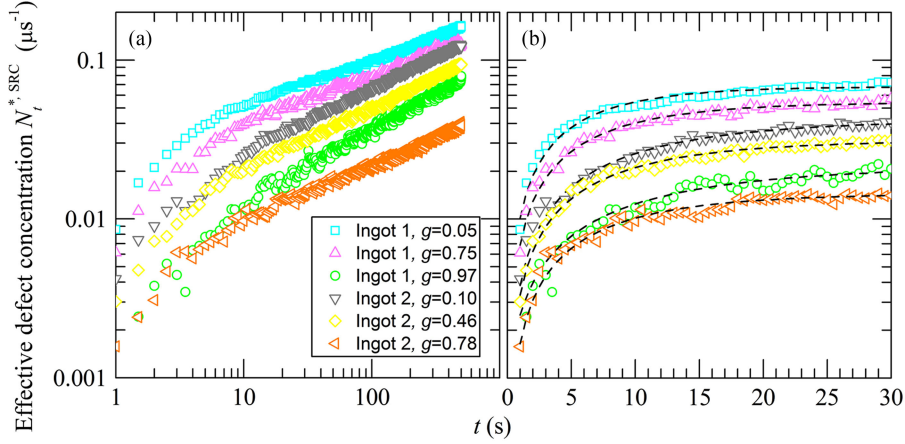5

Fig. 6.   (a) Extracted $N_t^{*,\mathrm{SRC}}(t)$ in several samples from both ingots. The fitting using data until 30 s is shown in dashed lines in (b).

The effective concentration of the SRC is inversely proportional to $\tau_{\mathrm{SRC}}(t) : N_t^{*,\mathrm{SRC}}(t) \propto 1/\tau_{\mathrm{SRC}}(t)$. The effective concentration of the SRC is proportional to the actual defect concentration, with the same, although unknown, scaling factor for all the samples. Note that $N_t^{*,\mathrm{SRC}}(t)$ obtained with the high-injection measurements are different from those obtained at low injection (injection of 10% of net doping) [1]. However, as shown above this method has the benefit of being dopant-density and dopant-type independent. The extracted $N_t^{*,\mathrm{SRC}}(t)$ of several samples from both ingots are shown in Fig. 6(a). The approximately parallel curves with different magnitudes indicate similar activation rate constants but different saturated concentrations of the SRC in those samples.

E. Stretched Exponential Activation Kinetics and the Simplified Fitting Method

Assuming the exponential relation for the activation kinetics of the SRC, we have [1]

$$N_t^{*,\mathrm{SRC}}(t) = N_t^{*,\mathrm{SRC,saturated}} \left[1 - \exp\left(-\frac{t}{\tau_{\mathrm{gen}}^{\mathrm{SRC}}}\right) \right] \quad (2)$$

where $N_t^{*,\mathrm{SRC,saturated}}$ is the effective saturated concentration of the SRC. When the injection level is steady, $\tau_{\mathrm{gen}}^{\mathrm{SRC}}$ is a constant over time. However, the spatially nonuniform injection level results in BO defects activated with different rate constants in different areas, as the BO defect can be activated by diffusing excess carriers as well as injected excess carriers [19]. As a result, the effective defect concentration $N_t^{*,\mathrm{SRC}}(t)$ shows a "stretched" exponential relation with time. This is evident at the longer time scales in Fig. 6(a).

To further demonstrate the stretched exponential kinetics, we show the fitting of $N_t^{*,\mathrm{SRC}}(t)$ with (2) for the sample from $g = 0.05$ of Ingot 1 in Fig. 7. Various upper time limits t_{up} in the range of 5–500 s until which the extracted data are fitted are set in the fitting. Fig. 7(a) shows the fitting when $t_{\mathrm{up}} = 30, 100,$ and 500 s. The average squared relative error and the extracted time constant in the fitting as functions of t_{up} are shown in Fig. 7(b) and (c), respectively.
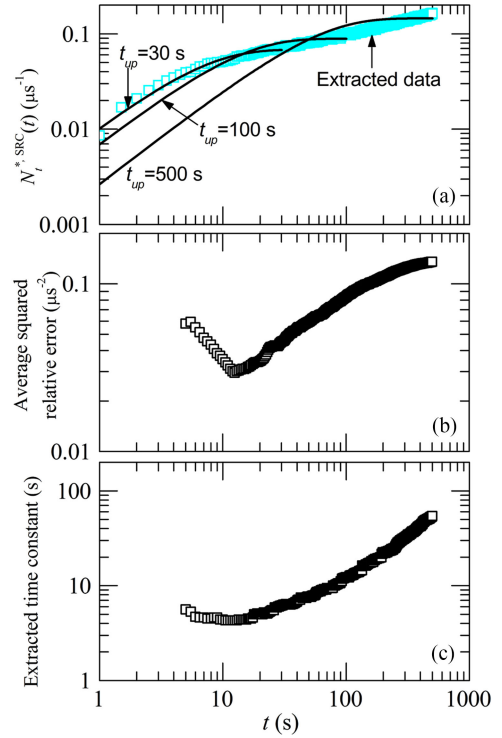

Fig. 7.   (a) Fitting $N_t^{*,\mathrm{SRC}}(t)$ with (2) for the sample from $g = 0.05$ of Ingot 1, when setting t_{up} as 30, 100, and 500 s. (b) Average squared relative error, and (c) Extracted time constant in the fitting, as functions of t_{up}.

In the studied area, the change in $N_t^{*,\mathrm{SRC}}(t)$ over a short time scale is dominated by the faster activation in the areas with higher injection levels, while over a longer time scale, the activation of the defects in the high-injection area tends to saturate, and the activation in the areas with lower injection begins to dominate. This explains the observed stretched exponential relations and is demonstrated by the fits shown in Fig. 7: when the data on a short time scale are fitted, the fitted activation time constant $\tau_{\mathrm{gen}}^{\mathrm{SRC}}$ is several seconds, in agreement with the predicted value (in Table II) at the highest injection level $\Delta n = 4 \times 10^{17}\ \mathrm{cm}^{-3}$ in the studied area. The reasonable fitting quality also indicates that in a short time scale, the activation in the high-injection
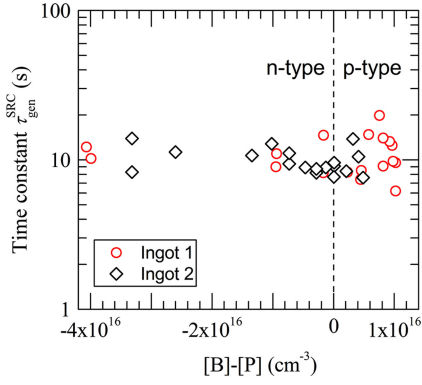
Fig. 8.   Activation time constant of SRC as a function of [B]–[P].

area is dominant and the slower activation in other areas is negligible. When the data on a longer time scale are fitted, the strongly increasing fitted $\tau_{\text{gen}}^{\text{SRC}}$ reflects the fact that the change in $N_t^{*,\text{SRC}}(t)$ is more dominated by the activation of the defects in the area with lower injection levels.

The reasonable fitting quality when fitting the data over the short time scale enables a convenient way to extract $\tau_{\text{gen}}^{\text{SRC}}$ and $N_t^{*,\text{SRC},\text{saturated}}$. As a simplified fitting method, in this work we only fit the extracted $N_t^{*,\text{SRC}}(t)$ over a short time scale, assuming a single exponential relation as expressed by (2). For all the samples, the best fitting quality is mostly achieved when $t_{\text{up}} =10$–30 s. When t_{up} is in this range, the extracted time constant does not vary significantly, as shown in Fig. 7(c). To lower the noise, we fix $t_{\text{up}} = 30$ s to allow more data points in the fitting. More detailed modeling of the stretched exponential kinetics on a longer time scale will be included in future work.

Fig. 6(b) shows the fitting of $N_t^{*,\text{SRC}}(t)$ for several samples from both ingots. Note that the simplification of the fitting method is unlikely to affect the main conclusions discussed in the following sections. The fact that similar PL signals were measured (see Fig. 5) demonstrates that the same high-injection distribution is achieved in different samples. Under this fixed high-injection condition, the defects are activated with approximately the same rate, as shown by the parallel curves in Fig. 6, which is clear no matter how the data are fitted. When the distribution of the activation rate constant is the same in different samples, the effective defect density at a time t is proportional to the saturated effective defect density: $N_t^{*,\text{SRC}}(t) \propto N_t^{*,\text{SRC},\text{saturated}}$. Therefore, although $N_t^{*,\text{SRC},\text{saturated}}$ was extracted with data only until 30 s (and is not saturated in some low-injection area), the comparison among different samples is reliable.

F. Analysis of the Activation Time Constant of SRC

The time constants $\tau_{\text{gen}}^{\text{SRC}}$ of all the Cz samples are shown in Fig. 8, as a function of [B]–[P]. $\tau_{\text{gen}}^{\text{SRC}}$ is approximately constant in different samples, indicating that the SRC has the same nature in both n- and p-Si with different doping levels or compensation levels. The average value of $\tau_{\text{gen}}^{\text{SRC}}$ is 10.5 s in all the samples. This agrees with the predicted values at the modeled highest

injection level $\Delta n = 3 \times 10^{17} - 4 \times 10^{17}$ cm^{-3} in the studied area, as shown in Table II.

Courtesy of the fixed carrier densities, the results help clarify the following issues: 1) The activation time constant $\tau_{\text{gen}}^{\text{SRC}}$ remains constant when $[\text{O}_i]$ varies in the range of $6 \times 10^{17} - 9 \times 10^{17}$ cm^{-3} in all the samples. The independence of $\tau_{\text{gen}}^{\text{SRC}}$ on $[\text{O}_i]$ is in agreement with the discussion in [6]. 2) $\tau_{\text{gen}}^{\text{SRC}}$ does not depend on [B] ([B] $\approx$ [B$_s$]). The dependence of the time constant on $[\text{B}_s]^2$ concluded in [6] actually reveals its dependence on the carrier densities. Our results show that the activation time constant is independent of n_0 and p_0, so the carrier densities could either be the total carrier densities n, p or the injection density Δn, Δp. A positive correlation between $\tau_{\text{gen}}^{\text{SRC}}$, and Δn, Δp, or n can be excluded based on [7] and [8]. The authors observed faster activation in p-type samples (where $\Delta n = \Delta p = n$) with higher [B$_s$], which have lower lifetimes and thus lower injection levels when the illumination intensity is fixed. Thus, we can confirm the dependence of $\tau_{\text{gen}}^{\text{SRC}}$ on the total hole concentration p, in agreement with [4] and [5]. The reasonable agreement with the predicted values (see Table II) based on [5] also indicates that the equations in [5] hold reasonably well for injection levels above 1×10^{17} cm^{-3}. However, we note that other authors have observed a saturated dependence of the time constant on the illumination intensities at relatively low-injection levels in p-type silicon [1], [20].

Furthermore, the independence of $\tau_{\text{gen}}^{\text{SRC}}$ on both $[\text{O}_i]$ and $[\text{B}_s]$ indicates that the previous model involving an oxygen dimer O_{2i} trapped by B$_s$ [1], [21], [22] is unlikely to be valid. This model was previously ruled out by other works, which reported that O_{2i} is not involved in the activation process [23], [24]. The other model which suggests that the activation of the BO defects is the reconfiguration from a latent state into a recombination-active state is more reasonable to explain the results obtained here [25], [26]. In this model, the latent defect complexes are formed after the ingot growth but before the light soaking [25]. So the defects can be activated with the same reaction rate constant when the same high-injection condition is provided, in spite of different defect concentrations.

G. Analysis of the Effective Saturated Concentration of SRC

The effective saturated defect concentration $N_t^{*,\text{SRC},\text{saturated}}$ (extracted from the fitting discussed in Section III-E) is normalized with $[\text{O}_i]^2$, and then plotted as a function of [B] in Fig. 9(a) and as a function of [B]–[P] in Fig. 9(b). The decreasing trend of the data shown in Fig. 9(a) rules out a positive correlation between $N_t^{*,\text{SRC},\text{saturated}}$ and [B] [2]. The normalized effective saturated defect concentration was also plotted as a function of the compensation ratio [27], but a much noisier trend was observed. The more likely dependence of $N_t^{*,\text{SRC},\text{saturated}}$ on [B]–[P] (net doping) can be concluded, as shown in Fig. 9(b). This conclusion is in agreement with the results reported in [2], [5], and [28]. This observation is against the B$_s$$-O_{2i}$ model, but agrees with those models where interstitial boron (B$_i$) instead of B$_s$ is involved [4], [25], [29]. The scattering of the data in Fig. 9(b) can be caused by noise and uncertainties in the PL

This article has been accepted for inclusion in a future issue of this journal. Content is final as presented, with the exception of pagination.

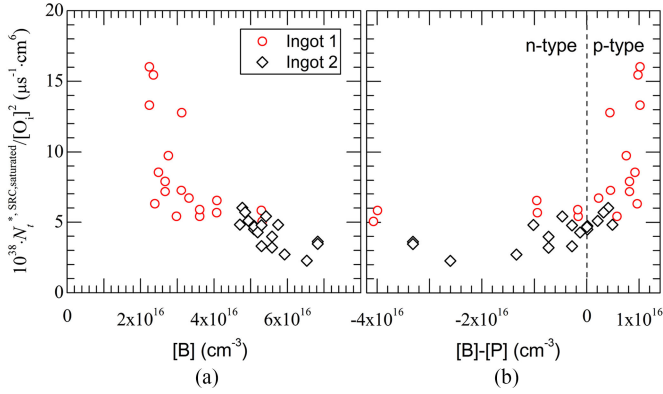SUN *et al.*: ACTIVATION KINETICS OF THE BORON–OXYGEN DEFECT IN COMPENSATED N- AND P-TYPE SILICON 7

Fig. 9. Effective saturated concentration of SRC normalized with $[O_i]^2$, as a function of [B] in (a), and as a function of [B]–[P] in (b).

measurements, as well as uncertainties in the predicted doping levels and the measured $[O_i]$.

can see from Fig. 9(b) that in n-Si, $N_t^{*,\mathrm{SRC,saturated}}$ is approximately constant, in agreement with the results reported by Schön *et al.* [5]. In p-Si, it increases with p_0. This agrees with the previous findings in [2], [5], and [28]. A gradual transition of the dependence on the net doping from n-Si to p-Si can be observed, which has not been shown conclusively before. By comparison, $N_t^{*,\mathrm{SRC,saturated}}$ (normalized with $[O_i]^2$) is always higher in p-Si than in n-Si with any doping level.

Note that the conclusions are based on observations in only *B- and P-doped silicon* in this work. The cases involving dopants other than B and P, such as Ga, are more complicated [30], [31]. In the case of Ga-doped silicon, apparently no BO defects will be formed in only Ga-doped silicon where p_0 can be as high as possible [6], yet it can still lead to the conclusion that the concentration of BO defects depends on [B] instead of p_0. A method to make the same conclusion hold in Ga and B codoped samples is to correct the defect concentration with the factor [B]/([B] + [Ga]), as discussed in [5].

When considering the results in this work and the literature including [2], [5], [28], [30], and [31], we suggest that the effects of the net doping on the saturated defect concentration are only indirect. For instance, assuming the model where interstitial boron B_i is involved leads to proportionality of the saturated defect concentration with $[B_i]$. Then, $[B_i]$ or the concentration of the relevant state of B_i could be affected by the Fermi level, which is related to the net doping [4], [32].

IV. CONCLUSION

The activation kinetics of the slow component of the BO defect (SRC) in compensated n- and p-type Cz-Si samples, with different doping levels and compensation levels, have been measured *in situ* using a micro-PL system under high-injection conditions. Besides significantly increasing the reaction rates, we have demonstrated that an advantage of this method is that it fixes a steady high-injection distribution over time and across all the samples. Courtesy of this, the time constant remains steady during the activation of the defects, and the activation rate

constant and defect concentration in differently doped samples can be compared without additional complications.

The SRC was found to have the same activation rate constant when fixing the high-injection level in n- and p-Si wafers with different net dopings. This helps to confirm that the rate constant depends only on the hole concentration, but not $[O_i]$ or [B]. The effective saturated concentration of the SRC normalized with $[O_i]^2$ remains constant in n-Si, and increases with the net doping in p-Si. A gradual transition of the dependence on the net doping from n-Si to p-Si was observed. The latent form reconfiguration model, instead of the $B_s - O_{2i}$ model, is more reasonable to explain the findings in this work.

REFERENCES

[1] J. Schmidt and K. Bothe, "Structure and transformation of the metastable boron-and oxygen-related defect center in crystalline silicon," *Phys. Rev. B*, vol. 69, 2004, Art. no. 024107.
[2] B. Lim, F. Rougieux, D. Macdonald, K. Bothe, and J. Schmidt, "Generation and annihilation of boron–oxygen-related recombination centers in compensated p- and n-type silicon," *J. Appl. Phys.*, vol. 108, 2010, Art. no. 103722.
[3] F. Rougieux *et al.*, "Influence of net doping, excess carrier density and annealing on the boron oxygen related defect density in compensated n-type silicon," *J. Appl. Phys.*, vol. 110, 2011, Art. no. 063708.
[4] V. Voronkov *et al.*, "Lifetime-degrading boron-oxygen centres in p-type and n-type compensated silicon," *J. Appl. Phys.*, vol. 110, 2011, Art. no. 063515.
[5] J. Schön *et al.*, "Characterization and modelling of the boron-oxygen defect activation in compensated n-type silicon," *J. Appl. Phys.*, vol. 118, 2015, Art. no. 245702.
[6] K. Bothe and J. Schmidt, "Electronically activated boron-oxygen-related recombination centers in crystalline silicon," *J. Appl. Phys.*, vol. 99, 2006, Art. no. 013701.
[7] B. Lim, "Boron–oxygen-related recombination centers in crystalline silicon and the effects of dopant-compensation," Ph.D. dissertation, Univ. Hannover, Hannover, Germany, 2012.
[8] R. Sondena *et al.*, "Electrical properties of compensated n- and p-type monocrystalline silicon," in *Proc. 26th Eur. Photovolt. Sol. Energy Conf. Exhib.*, Hamburg, Germany, 2011, pp. 1824–1828.
[9] T. Niewelt *et al.*, "Fast in-situ photoluminescence analysis for a recombination parameterization of the fast BO defect component in silicon," *J. Appl. Phys.*, vol. 120, 2016, Art. no. 085705.
[10] T. Niewelt *et al.*, "Electrical characterization of the slow boron oxygen defect component in Czochralski silicon," *Phys. Status Solidi-Rapid Res. Lett.*, vol. 9, pp. 692–696, 2015.
[11] T. Niewelt, J. Schön, W. Warta, S. W. Glunz, and M. C. Schubert, "Degradation of crystalline silicon due to boron–oxygen defects," *IEEE J. Photovolt.*, vol. 7, no. 1, pp. 383–398, Jan. 2017.
[12] W. Shockley and W. Read Jr., "Statistics of the recombinations of holes and electrons," *Phys. Rev.*, vol. 87, pp. 835–843, 1952.
[13] R. N. Hall, "Electron-hole recombination in germanium," *Phys. Rev.*, vol. 87, 1952, Art. no. 387.
[14] C.-T. Sah and W. Shockley, "Electron-hole recombination statistics in semiconductors through flaws with many charge conditions," *Phys. Rev.*, vol. 109, 1958, Art. no. 1103.
[15] J. Härkönen *et al.*, "Recovery of minority carrier lifetime in low-cost multicrystalline silicon," *Sol. Energy Mater. Sol. Cells*, vol. 73, pp. 125–130, 2002.
[16] P. Gundel *et al.*, "Quantitative carrier lifetime measurement with micron resolution," *J. Appl. Phys.*, vol. 108, 2010, Art. no. 033705.
[17] H. Sio *et al.*, "Quantifying carrier recombination at grain boundaries in multicrystalline silicon wafers through photoluminescence imaging," *J. Appl. Phys.*, vol. 116, 2014, Art. no. 244905.

[18] T. Trupke and R. Bardos, "Photoluminescence: A surprisingly sensitive lifetime technique," in *Proc. 31st IEEE Photovolt. Spec. Conf.*, 2005, pp. 903–906.

[19] T. U. Nærland *et al.*, "The role of excess minority carriers in light induced degradation examined by photoluminescence imaging," *J. Appl. Phys.*, vol. 112, 2012, Art. no. 033703.

[20] H. Hashigami *et al.*, "Effect of illumination conditions on Czochralski-grown silicon solar cell degradation," *J. Appl. Phys.*, vol. 93, pp. 4240–4245, 2003.

[21] J. Adey *et al.*, "Degradation of boron-doped Czochralski-grown silicon solar cells," *Phys. Rev. Lett.*, vol. 93, 2004, Art. no. 055504.

[22] D. W. Palmer *et al.*, "Kinetics of the electronically stimulated formation of a boron-oxygen complex in crystalline silicon," *Phys. Rev. B*, vol. 76, 2007, Art. no. 035210.

[23] V. V. Voronkov *et al.*, "Light-induced lifetime degradation in boron-doped Czochralski silicon: Are oxygen dimers involved?" *Energy Procedia*, vol. 38, pp. 636–641, 2013.

[24] L. I. Murin *et al.*, "The oxygen dimer in Si: Its relationship to the light-induced degradation of Si solar cells?" *Appl. Phys. Lett.*, vol. 98, 2011, Art. no. 182101.

[25] V. V. Voronkov and R. Falster, "Latent complexes of interstitial boron and oxygen dimers as a reason for degradation of silicon-based solar cells," *J. Appl. Phys.*, vol. 107, 2010, Art. no. 053509.

[26] V. Voronkov and R. Falster, "The nature of boron-oxygen lifetime-degrading centres in silicon," *Phys. Status Solidi C*, vol. 13, pp. 712–717, 2016.

[27] J. Geilker *et al.*, "Light-induced degradation in compensated p-and n-type Czochralski silicon wafers," *J. Appl. Phys.*, vol. 109, 2011, Art. no. 053718.

[28] D. Macdonald *et al.*, "Light-induced boron-oxygen defect generation in compensated p-type Czochralski silicon," *J. Appl. Phys.*, vol. 105, 2009, Art. no. 093704.

[29] D. Macdonald *et al.*, "The impact of dopant compensation on the boron-oxygen defect in p- and n-type crystalline silicon," *Physica Status Solidi A*, vol. 208, pp. 559–563, 2011.

[30] M. Forster *et al.*, "Boron-oxygen defect in Czochralski-silicon co-doped with gallium and boron," *Appl. Phys. Lett.*, vol. 100, 2012, Art. no. 042110.

[31] M. Forster *et al.*, "Impact of compensation on the boron and oxygen-related degradation of upgraded metallurgical-grade silicon solar cells," *Sol. Energy Mater. Sol. Cells*, vol. 120, pp. 390–395, 2014.

[32] R. Harris *et al.*, "Negative-U defect: Interstitial boron in silicon," *Phys. Rev. B*, vol. 36, 1987, Art. no. 1094.

Authors' photographs and biographies not available at the time of publication.